Arabian Journal of Chemistry (2023) **16**, 105145

King Saud University

Arabian Journal of Chemistry

www.ksu.edu.sa
www.sciencedirect.com

ORIGINAL ARTICLE

Characterization of new modified mesostructured silica nanocomposites fabricated for effective removal of aromatic acids

Zheng-Zhe Li [a], Tzong-Horng Liou [a,b,*], Wen-Yang Liu [a], Chun-Chia Hsu [a], Sheng-En Chiu [a]

[a] *Department of Chemical Engineering, Ming Chi University of Technology, 84 Gungjuan Rd., Taishan, New Taipei 24301, Taiwan*
[b] *Battery Research Center of Green Energy, Ming Chi University of Technology, 84 Gungjuan Rd., Taishan, New Taipei 24301, Taiwan*

Received 26 April 2023; accepted 6 July 2023
Available online 11 July 2023

KEYWORDS

Mesostructured silica;
Surface modification;
Characterization;
Aromatic acid;
Recycling

Abstract Santa Barbara Amorphous-15 (SBA-15) is a mesoporous molecular sieve with a large surface area and is extensively applied in purification, separation, and catalytic procedures. In this study, an SBA-15 was prepared from a sodium silicate precursor, and pentaethylene hexamine was anchored to its surface. A composite named N-SBA-15 was characterized using several experimental techniques. FTIR and XPS measurements confirmed that amino groups were conjugated on the surface of SBA-15. XRD and TEM confirmed that N-SBA-15 comprised highly ordered, hexagonal mesopore structures, which were not destroyed by the addition of amino groups. After functionalization, the surface area, pore volume, and pore size of the composite were 188 m^2/g, 0.303 cm^3/g, and 5.0 nm, respectively. N-SBA-15 was applied in the adsorption of aromatic acids, namely tannic acid (TA), acid red 1 (AR-1), and acid blue 40 (AB-40). The influence of various adsorption conditions such as dye concentration, adsorbent dosage, solution pH, and solution temperature was investigated. For AB-40 dye, the N-SBA-15 composite exhibited 40 times higher adsorption capacity than pure SBA-15. The highest adsorption capacities of N-SBA-15 for TA, AB-40, and AR-1 were 869, 818, and 308 mg/g, respectively. Thermodynamic studies were conducted to evaluate the exothermic property of the adsorption process and spontaneous behavior. The adsorptive data fitted well with pseudo-second-order and Langmuir isotherm models. Results confirmed that amino-modified SBA-15 material is a promising adsorbent for the elimination of aromatic acids

* Corresponding author at: Department of Chemical Engineering, Ming Chi University of Technology, 84 Gungjuan Rd., Taishan, New Taipei 24301, Taiwan.
E-mail address: thliou@mail.mcut.edu.tw (T.-H. Liou).

Peer review under responsibility of King Saud University. Production and hosting by Elsevier.

Production and hosting by Elsevier

https://doi.org/10.1016/j.arabjc.2023.105145

form aqueous solution.

1. Introduction

Silica (SiO_2) is a mechanically strong, nontoxic, and hydrophobic material that has wide applications in the pharmaceutical, food, and polymer industries (Razak et al., 2022). SBA-15 is a mesoporous silica material composed of a two-dimensional, highly ordered hexagonal structure. The material contains uniform mesopores and has a high surface area and high stability, which rendering it suitable for applications in fuel cell operation (Rajabi et al., 2021), CO_2 adsorption (Wang et al., 2023a), drug delivery (Ulagesan et al., 2022), tissue engineering (Vargas-Osorio et al., 2022), catalysis (Sfeir et al., 2023; Al-Nayili et al., 2022), and adsorption (Sadeghi et al., 2023). At present, there are many compounds such as SBA-15, metal − organic framework (MOFs), TiO_2, C_3N_4, perovskite, MCM-41, and MCM-48 can be used as adsorbent materials (Bi et al., 2022; Bi et al., 2023; Zhang et al., 2022a; Yang et al., 2022; Li et al., 2023; Atiyah, et al., 2022). In particular, SBA-15 possesses adjustable pore size, regular array of channel structures, and large mesopores (pore size, 10–30 nm), making the material a potential adsorbent for capturing large molecular compounds for reducing mass transfer resistance (Zhou et al., 2022a). The property of materials is often affected by different fabrication methods (Zhang et al., 2023a). Conventionally, SBA-15 is synthesized through hydrothermal treatment of a silicon precursor and surfactant template in a strong acidic medium (Sadou et al., 2022). Although SBA-15 can be synthesized with tetraethlyorthosilicate (TEOS) as the silicon source, the high cost of TEOS leads to an increase in overall production costs. Sodium silicate (Na_2SiO_3) is a cost-effective alternative that can be used for the synthesis of SBA-15, thereby reducing the overall expense of raw material for mass production. Accordingly, a cost-effective approach for producing SBA-15 nanomaterials from a sodium silicate precursor is required.

Aromatic acids such as tannic acid (TA), acid red 1 (AR-1), and acid blue 40 (AB-40) are typical organic compounds that are often used in food, leather, textile, paper, and plastic industries (Shi et al., 2022). Yearly dye production is estimated at 700,000 tons, and the majority of waste dyes are released into rivers and streams without treatment (Souza et al., 2021). Organic pollutants in drinking water, even in small concentrations, may be harmful to human health and environmental safety. Therefore, the controlled discharge of organic pollutants from wastewater is a vital environmental concern. Numerous physical and chemical techniques have been used to treat aqueous solutions and separate organic pollutants and toxic substances from them, such as adsorption, photocatalysis, microwave catalysis, advanced oxidation, biological processes, ion exchange, and membrane filtration (Wang et al., 2022; Li et al., 2023; Yu et al., 2023; Lin et al., 2023; Al-Jaaf et al., 2022; Ali et al., 2022a; Kadhum et al., 2021; Alardhi et al., 2020). Most of these techniques present some disadvantages including high cost, complicated operation, and foul smell. Adsorption is regarded as the most efficient method because of the low investment required, simplicity of use, and relatively low sludge generation (Osagie et al., 2021). It is a well-known equilibrium separation process, which does not cause the formation of harmful substances. Because of its ability to remove various kinds of organic pollutants, the adsorption process can produce high quality treated water.

Ordered mesoporous silica materials have been successful applied in environmental water treatment over the past few decades. However, these materials are negatively charged because the isoelectric point is in the range 2.5—4 and the surface Si-OH is partially deprotonated under neutral conditions. This condition is unfavorable for the adsorption of anionic pollutants. Chemical modification of mesoporous silica materials with amino groups enhances their adsorption efficiency. Hybrid organic–inorganic materials have the benefits of a high-strength silica framework (includes high porosity and large surface area) and high binding capacity to pollutants (i.e., amino groups). Gao et al. (Gao et al., 2020) prepared an amino-functionalized metal organic framework through hydrothermal synthesis. Functionalization can promote the formation of Lewis base sites, which effectively enhance the elimination of anthraquinone and azo dyes. Perrotti et al. (2019) used green iron nanoparticles on amino-functionalized SiO_2 for support. The highest removal efficiency of 100% was achieved for methyl orange dye. The addition of iron can improve the stability and recycling capacity of related composites. Zhang et al. (2018) synthesized mesoporous SBA-15 and modified its surface with amino and Fe^{3+} groups. When the Fe^{3+} concentration was increased from 3.93% to 8.26%, the maximum adsorption capacity for tetracycline increased from 102 to 188 mmol/kg. Kalhor et al. (2018) fabricated a silica nano hollow sphere and modified it by using amino compounds. The modified composite achieved a maximum adsorption of 10 mg/g for imidacloprid pesticide. Anbia and Salehi (2012) used the amino-supported silica materials SBA-3 and 3-aminopropyltriethoxysilane (SBA-3/APTES) and pentaethylene hexamine (SBA-3/PEHA) to remove acid dyes. SBA-3/APTES showed lower adsorption capacity than did SBA-3/PEHA.

Numerous studies have already reported the preparation of adsorbents from microporous/mesoporous materials. However, the preparation procedures of these adsorbents are much more complicated compared with the present work. In addition, sodium silicate is a low-cost source that can reduce the overall expense of raw material. There is a lack of information in the literature about surface modification of SBA-15 by using PEHA and silicate sodium precursor for obtaining high adsorption capacity materials. This lack in existing literature is a motivation for the present study. The principal aim of this study was to develop an amino-functionalized SBA-15 mesoporous material for eliminating organic pollutants from water that has potential benefits for large-scale application (Jabbar et al., 2022). TA, AR-1, and AB-40 were chosen as the model anionic adsorbates to examine the adsorption activity of the composite materials. The study procedure was as follows: (1) SBA-15 was fabricated through the hydrothermal method by using sodium silicate and surfactant precursors. In addition, the effect of hydrothermal treatment time and temperature on the structure of mesoporous silica was investigated. (2) PEHA was added to mesoporous silica to coat amino groups onto the surface of SBA-15. (3) The effects of organic pollutants on the adsorption capacity of SBA-15 before and after functionalization were compared. (4) The effects of adsorption conditions, including dye concentration, adsorbent dosage, solution pH, and solution temperature, on the adsorption efficiency of the modified SBA-15 material were evaluated. (5) The thermodynamic, isotherm, and kinetics models were employed to investigate the spontaneous behavior and adsorption mechanism. Furthermore, the physicochemical features of SBA-15 before and after amination were evaluated.

2. Materials and methods

2.1. Materials

Ethanol (99.9 wt%), sodium hydroxide, sulfuric acid, hydrochloric acid, and PEHA were obtained from Merck (Gernsheim, Germany). AR-1 ($C_{18}H_{13}N_3Na_2O_8S_2$, 509.42 g/mol), AB-40 ($C_{22}H_{16}N_3NaO_6S$, 473.4 g/mol), TA ($C_{76}H_{52}O_{46}$, 1701 g/mol), pluronic triblock copolymer (P123,

$EO_{20}PO_{70}EO_{20}$), and sodium silicate [$Na_2O(SiO_2)_x(H_2O)_x$, $SiO_2 \sim 26.5$ wt%, $Na_2O \sim 10.6$ wt%] were acquired from Sigma-Aldrich (Taufkirchen, Germany). High-purity (99.995%) mixed gas (79% N_2 and 21% O_2) was acquired from Sun Fu (Taipei, Taiwan). The molecular structures of AR-1, AB-40, and TA are shown in Fig. 1.

2.2. Preparation of SBA-15

SBA-15 was prepared through hydrothermal treatment (Liou et al., 2021; Liou et al., 2023), in which 4.0 g of P123 is added to 105 mL of 1.6 M HCl solution at 35 °C and mixed through magnetic stirring. Subsequently, 8.26 g of sodium silicate was added to 50 g of deionized water, and the mixture was placed in P123 solution and agitated at 35 °C for 15 min. The suspension was maintained at 35 °C for 24 h; it was then placed in a Teflon cup for processing in an autoclave. After the hydrothermal reaction proceeded at 100 °C for 24 h, the sample was washed with water, filtered, and dried at 60 °C. The prepared SBA-15 was then assembled by calcining the powder at 550 °C for 6 h in mixed gas to remove the organic template.

2.3. Preparation of N-SBA-15

Amino-functionalized SBA-15 was synthesized following the procedure. In brief, SBA-15 was heated in air at 100 °C for 24 h to remove moisture. Subsequently, PEHA (1.0 g) was added to an ethanol solution (50.0 g) at room temperature and stirred for 40 min. SBA-15 (2.0 g) was then added to the PEHA solution in a round-bottom flask, and the mixture was heated at 80 °C for 4 h by using a reflux apparatus. Thereafter, the specimen was dried at 100 °C, and the final product was labeled as N-SBA-15. Fig. 2 shows a schematic representation for synthesis of amino-functionalized SBA-15 specimens.

2.4. Specimen characterization

The surface area and pore distribution of the specimens were estimated at − 196 °C by using a N_2 adsorption instrument (Micrometrics, ASAP 2020, Norcross, GA, USA). The functional groups before and after the amination of silica were observed with a Shimadzu FTIR-8300 analyzer (Nakagyo-ku, Kyoto, Japan). The low-angle (0.5° to 5°) and high-angle (10° to 70°) XRD data of the silica specimens were analyzed through Cu-kα radiation by using an X'pert Pro diffractometer (PANalytical, Malvern, UK), with an operating voltage of 45 kV and current of 40 mA. The SBA-15 mesostructures and surface morphologies were characterized using transmission electron microscopy (TEM; model JEM-2100, JEOL, Akishima, Tokyo, Japan) and scanning electron microscopy (SEM; model S-3400 N, HITCHI, Chiyoda, Tokyo, Japan). Thermogravimetric analysis (TGA) was used to realize the thermal stability of silica specimens in a TA apparatus (model TGA/SDTA851e; Mettler Toledo, Ohio, USA). W/Wo denoted the residual weight of the specimen. The Si, C, N, and O atoms that appeared on the N-SBA-15 surface were

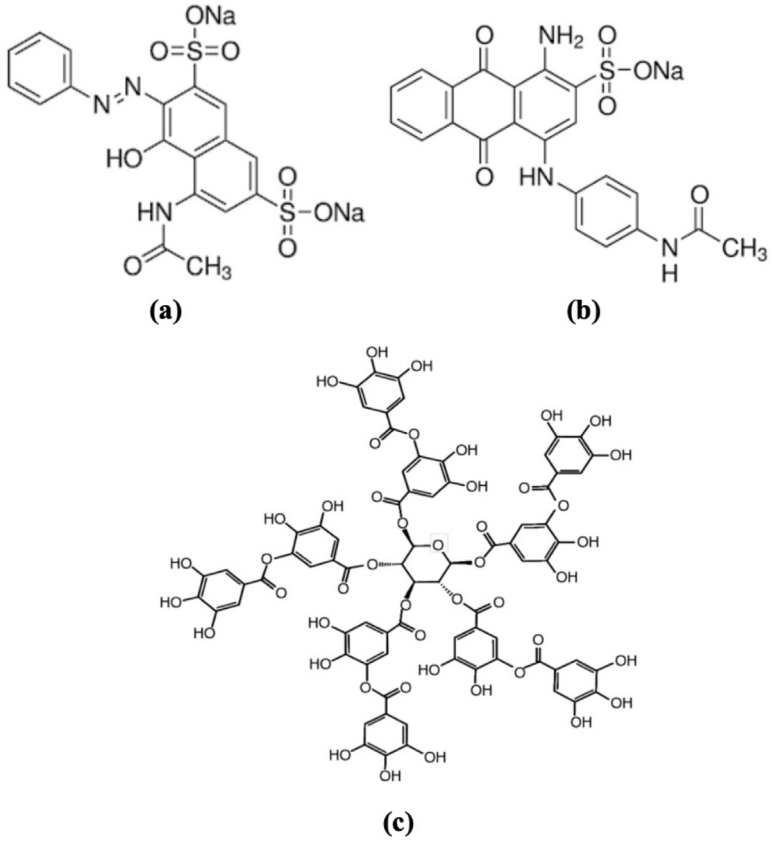

Fig. 1 Structures of (a) AR-1, (b) AB-40, and (c) TA.

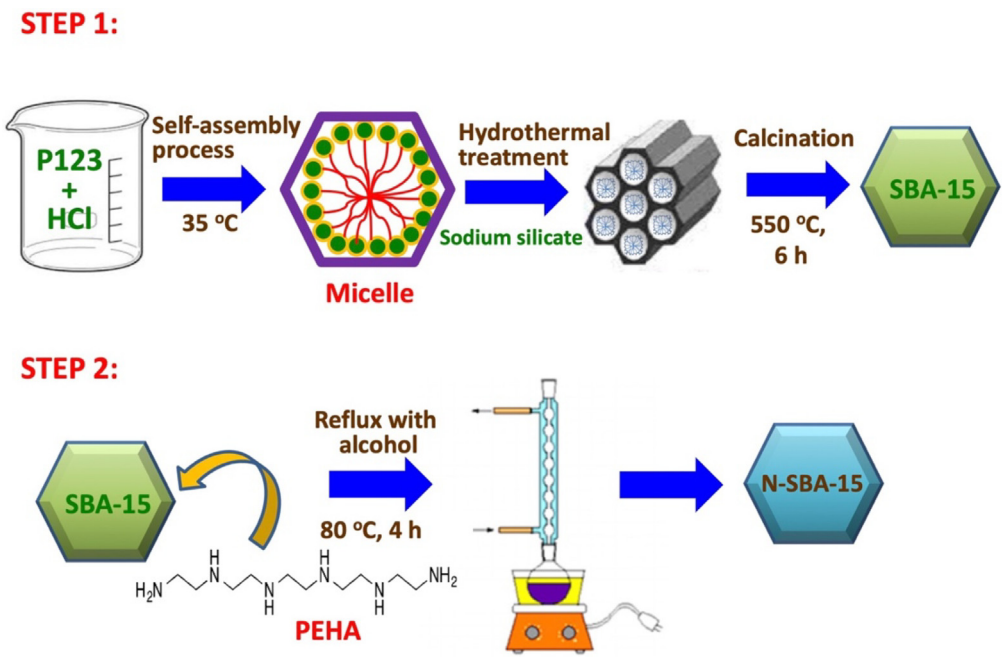

Fig. 2 Schematic representation of SBA-15 and N-SBA-15 synthesis.

observed through X-ray photoelectron spectroscopy (XPS; Escalab 250 Xi, Thermo Scientific, Waltham, MA, USA).

2.5. Adsorption tests

Adsorption experiments were conducted in a batchwise manner (Liou et al., 2022). Typically, 10 mg of N-SBA-15 was mixed with 50 mL of adsorbate solution (containing TA, AR-1, and AB-40). The solution temperature and agitation speed were set as 25 °C and 150 rpm, respectively. The adsorption conditions varied in this study, including solution temperature (25, 35, and 45 °C), pH value (2, 4, 6, 8, 10, and 12), adsorbent dosage (5, 10, 15, 20, and 25 mg), and initial adsorbate concentration (40, 60, 80, 100, and 120 mg/L). The solution pH was modified by the addition of 0.1 M NaOH or HCl and measured using a pH meter (Metter S20ks). After 0–120 min, the remaining solution was collected through membrane filtration and analyzed using an ultraviolet–visible Genesys spectrophotometer (Thermo Electron Corporation, Waltham, MA, USA). A standard solution was used to calibrate the UV spectrophotometer for every analysis. The calibration curves were used to determine the TA, AR-1, and AB-40 concentrations. For each adsorption experiment, the TA and dye concentrations were tested at least three times. The amounts of adsorbed acids (q_t, mg/g) and removal efficiency (R, %) of the N-SBA-15 were calculated using the following equations (Yin et al., 2022).

$$q_t = \frac{(C_o - C)V}{W} \quad (1)$$

$$R = \frac{C_o - C}{C_o} x100 \quad (2)$$

where C_o and C_t (mg/L) are the acid concentrations at the initial and specific times, V (L) is the solution volume, and W (g) is the weight of N-SBA-15.

3. Results and discussion

3.1. Mesoporous and crystalline phases of the silica specimens

SBA-15 is synthesized by the interaction between silicate species and a surfactant template. The hydrothermal treatment temperature and treatment duration are the key factors affecting the formation of silica pore frameworks. The low-angle XRD curves of pure SBA-15 materials that underwent hydrothermal treatment for 0–48 h are displayed in Fig. 3a. The corresponding diffraction peaks at (1 0 0), (1 1 0), and (2 0 0) planes were ascribed to the presence of well-ordered mesopores and a 2D hexagonal SBA-15 structure (Zhang et al., 2023b). The (1 1 0) and (2 0 0) peaks were well resolved at the later time points, suggesting that increasing the hydrothermal treatment time favored the construction of the hexagonal mesopores with a highly ordered array. Moreover, the peak at (1 0 0) was shifted to lower angles as the hydrothermal time increased, suggesting a slight increase in d-spacing, as observed by Souza et al (2021). As shown in Fig. 3b, when the temperature was further increased to 130 °C, the (2 0 0) peak disappeared; this disappearance may have been caused by the destruction of micelles, consequently forming a poorly ordered mesostructure. Accordingly, the optimum hydrothermal treatment time and temperature were 48 h and 100 °C, respectively. The XRD pattern of N-SBA-15 (Fig. 3c) revealed three diffraction peaks at the (1 0 0), (1 1 0), and (2 0 0) planes, confirming that the ordered array of the hexagonal structure of N-SBA-15 was maintained. The high-angle XRD patterns for SBA-15 and N-SBA-15 exhibited a wide peak at $2\Theta = 20°–30°$ (Fig. 3d), indicating a characteristic of amorphous materials (Liu et al., 2022).

3.2. Nitrogen sorption measurement and pore analysis

The nitrogen sorption isotherms of SBA-15 and N-SBA-15 specimens are illustrated in Fig. 4. Fig. 4a and Fig. 4c show

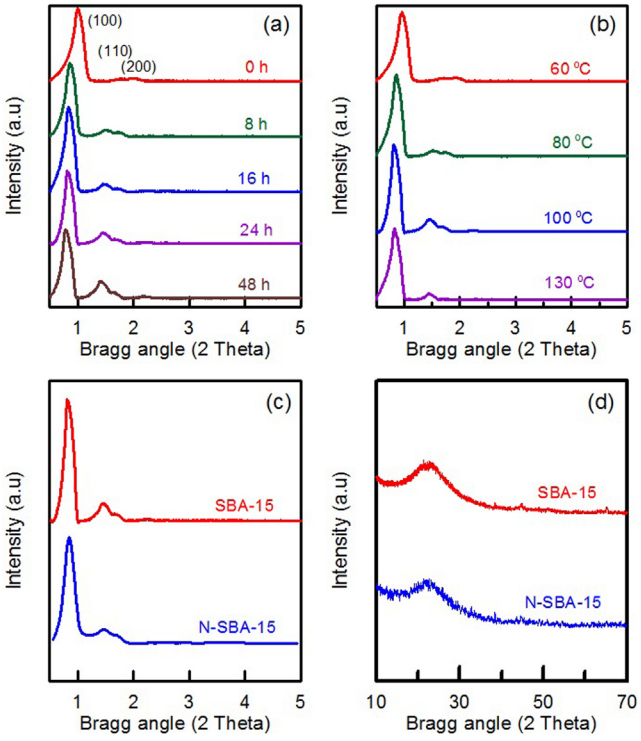

Fig. 3 XRD curves of SBA-15 materials: (a) hydrothermal treatment time and (b) hydrothermal treatment temperature. XRD curves of SBA-15 and N-SBA-15: (c) low angle and (d) wide angle.

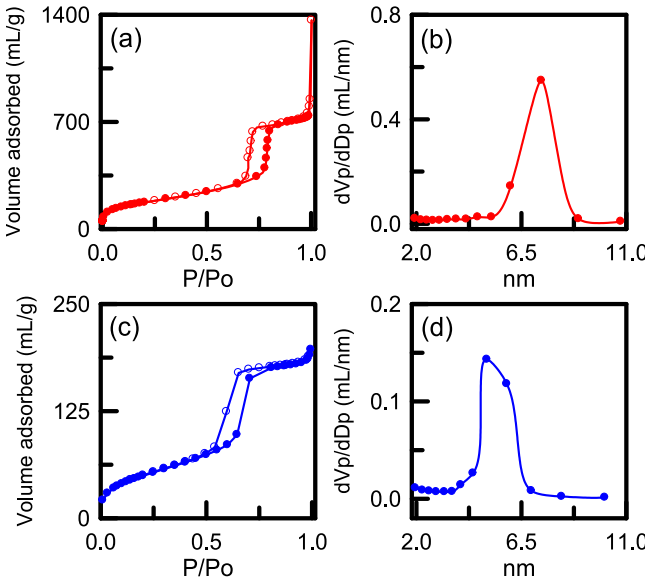

Fig. 4 Nitrogen adsorption–desorption isotherm and pore size distribution: (a) and (b) SBA-15; (c) and (d) N-SBA-15.

the two specimens corresponding to a type IV isotherm with a type H1 structure of mesoporous material (Zhang et al., 2023c). The two curves had similar hysteresis loops, implying that the incorporation of amino groups did not destroy the SBA-15 framework. However, the adsorbed volume of N_2 was markedly decreased after the amination process. Fig. 4b and Fig. 4d show that SBA-15 and N-SBA-15 had pore sizes of 7.4 and 5.0 nm, respectively, indicating that the mesopore size was reduced after functionalization. Table 1 displays the physisorption data of the silica specimens before and after amination. Pure SBA-15 had a BET surface area of 615 m^2/g, whereas the surface area of the amino-modified SBA-15 was substantially decreased to 188 m^2/g. The incorporation of amino groups caused a 70% reduction in surface area. Moreover, the total pore volumes decreased from 1.132 to 0.307 cm^3/g, which was attributable to the loss of mesopore volume after functionalization, most likely because the pores were filled by the amino groups. The mesopore fraction of the two silica samples was in the range of 98.70% to 99.29%, which slightly decreased after the addition of the amino groups.

3.3. SEM and TEM analysis of silica specimens

SEM images of the amino-modified and unmodified SBA-15 are presented in Fig. 5. Pure SBA-15 (Fig. 5a) comprised agglomerates of small particles with a rod-like morphology, as reported by a previous study (Wang et al., 2023b). The diameters and lengths of the particles (Fig. 5b) ranged from 250 to 600 nm and 800 to 2.6 μm, respectively. The morphology of N-SBA-15 (Fig. 5c and Fig. 5d) did not vary obviously after functionalization, which is in agreement with the findings in the literature (Fei et al., 2016). However, the addition of PEHA reduced the particle size of N-SBA-15, with the diameter and length of the particles ranging from 200 to 600 nm and 650 to 1.3 μm, respectively.

TEM was used to investigate the changes in the microstructure of SBA-15 after an amination reaction. Pure SBA-15 exhibited parallel pore channels (Fig. 6a) and ordered mesopores arranged in a hexagonal symmetry (Fig. 6b). Furthermore, SBA-15 exhibited a large hexagonal particle size (Fig. 6c). The self-assembly of surfactant templates resulted in a honeycomb-like structure in pure SBA-15. After modification with the amino groups, N-SBA-15 (Fig. 6d) displayed the same morphology as that observed in the pure SBA-15 sample. In addition, the pore size was reduced. This reduction in pore diameter was caused by the surface coating of amino compounds on the pore walls of silica.

3.4. Characterization of the silica specimens

The FTIR spectra for SBA-15 before and after amination are presented in Fig. 7a. In general, pure SBA-15 displayed Si-OH vibrations at 3200–3500, 1635, and 980 cm^{-1}. The strong peak at 1090 cm^{-1} corresponded to stretching of symmetrical and antisymmetrical Si-O-Si vibrations. The bending vibrations of Si-O-Si were observed at the bands of 450 and 790 cm^{-1} (Chen et al., 2023). The three bands at 1572, 1499, and 610 cm^{-1} in the adsorption spectrum for N-SBA-15 were related to the stretching vibrations of amino groups. The peaks observed at 2850–3000 and 1450 cm^{-1} possibly denoted a $-CH_3$ group. The results confirmed that amino groups were successfully conjugated with SBA-15. Furthermore, the bands at 3250–3450 cm^{-1} may be related to the $-NH_2$ groups, as

Table 1 Surface area and pore characteristics of prepared samples.

Sample	S_{BET} (m^2/g)	V_t (cm^3/g)	V_{mic} (cm^3/g)	V_{meso} (cm^3/g)	V_{meso}/V_t (%)	d_P (nm)
SBA-15	615	1.132	0.008	1.124	99.29	7.4
N-SBA-15	188	0.307	0.004	0.303	98.70	5.0

S_{BET} = specific surface area, V_t = total pore volume, V_{mic} = micropore volume, V_{meso} = mesopore volume, dp = pore diameter (BJH desorption).

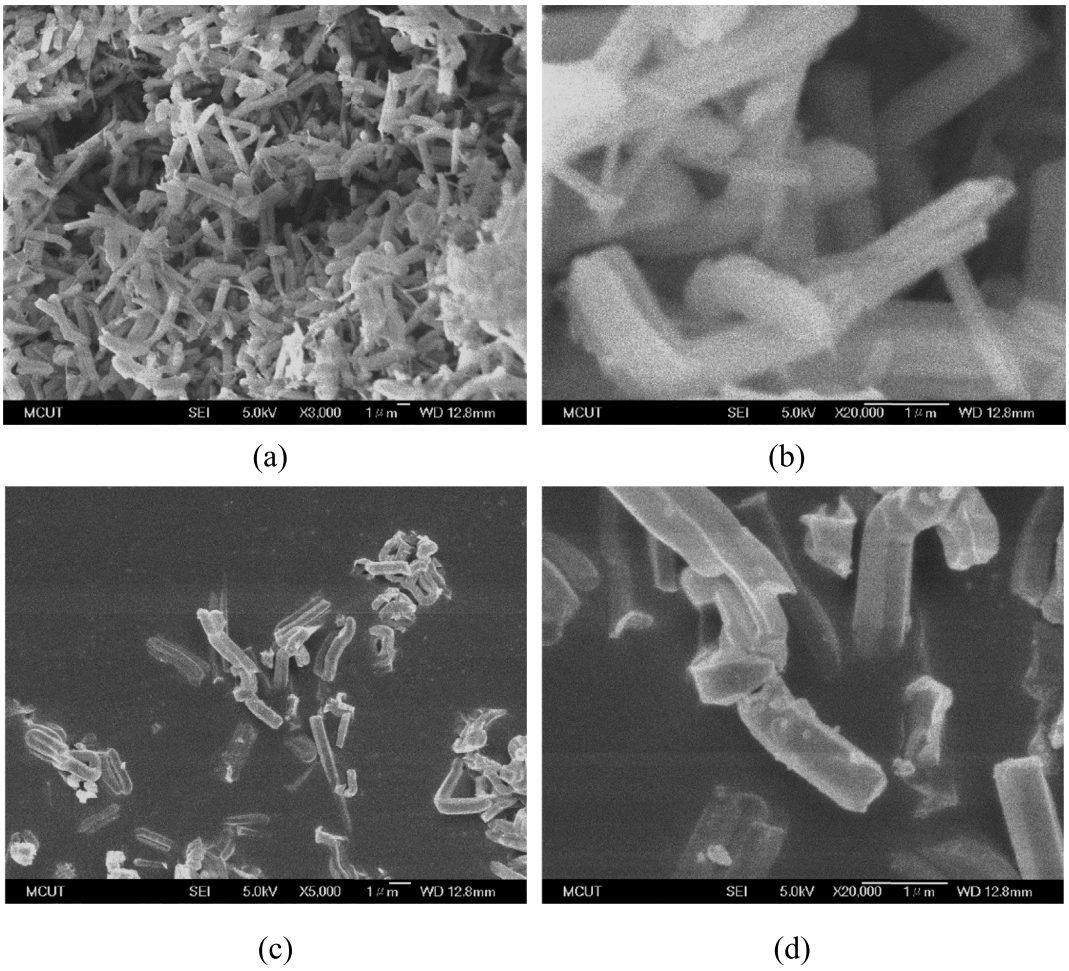

Fig. 5 SEM images: (a) and (b) SBA-15; (c) and (d) N-SBA-15.

reported by Anbia and Salehi (2012). However, $-NH_2$ groups were not easily found on the spectrum, possibly because the functional groups were hidden by –OH groups. The thermal stability of SBA-15 before and after amination was evaluated using TGA (Fig. 7b). Pure SBA-15 did not display obvious mass loss, indicating good thermal stability in the studied temperature range. However, the amino-functionalized SBA-15 exhibited more significant mass loss of approximately 26.09 wt% in the temperature range between 200 and 700 °C. The mass loss was caused by thermal decomposition of amino groups, confirming the presence of PEHA in the SBA-15 material. Moreover, no obvious mass loss was observed when the temperature exceeded 700 °C.

The surface chemistry of N-SBA-15 was evaluated through XPS. The main peaks in the survey spectrum indicated the presence of Si, C, N, and O elements (Fig. 8a). The results suggested that N-SBA-15 comprised SiO_2 as the solid component and an amino group. The N1s spectrum in Fig. 8b displayed two types of chemical bonds of the amino group ($-NH_2$ and $-NH_3^+$) on the composite surface, which were centered at 405.2 and 399.5 eV, respectively (Wang et al., 2010). The C1s spectrum in Fig. 8c exhibited two peaks at 284.8 and 290.9 eV, which were related to C–C bonds from the amino group, respectively (Gao et al., 2020). These results confirmed that the amino group was coated on the SBA-15 surface.

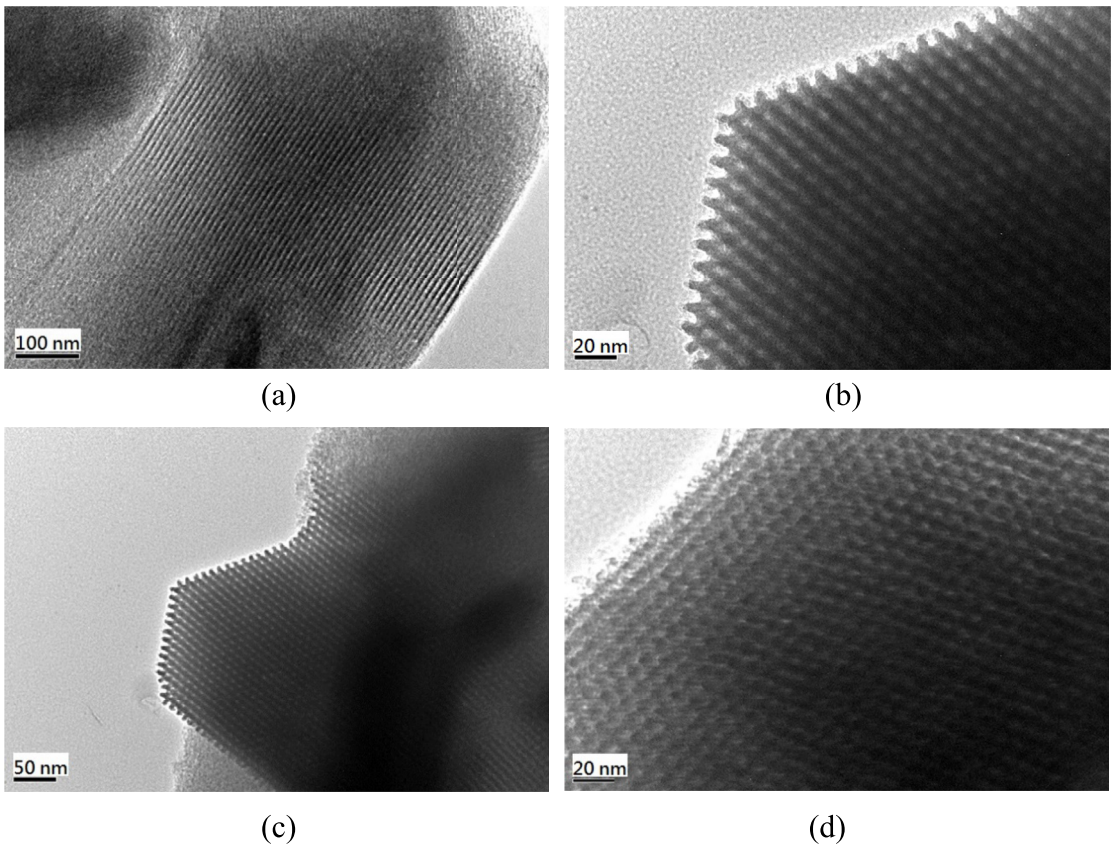

Fig. 6 TEM images: (a) - (c) SBA-15 and (d) N-SBA-15.

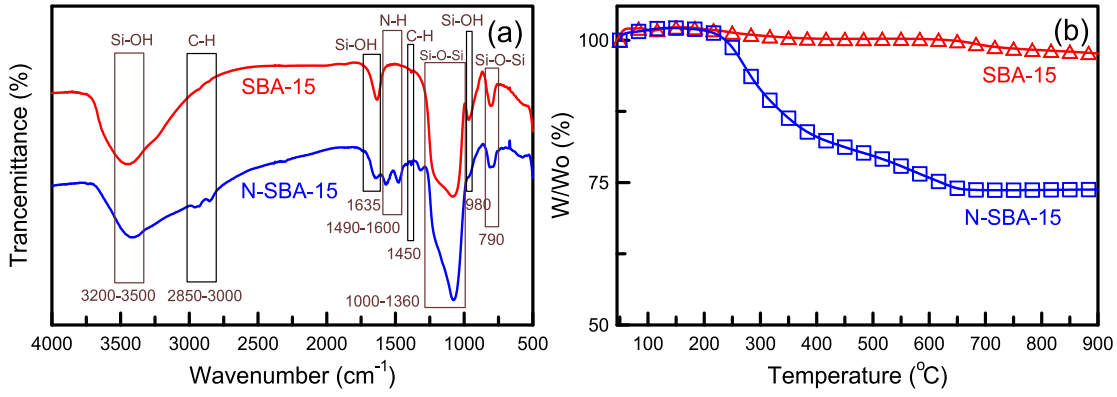

Fig. 7 (a) FTIR patterns and (b) TGA data of SBA-15 and N-SBA-15.

3.5. Adsorption experiments

3.5.1. Effects of contact time

The influence of contact time on the adsorption capacity of N-SBA-15 was estimated in relation to three anionic compounds: TA, AR-1, and AB-40. For AB-40. The adsorption capacity of N-SBA-15 was 40 times higher than that of pure SBA-15 (q_e = 410 mg/g vs 10 mg/g; Fig. 9). This observation proved that a combination of amino groups and mesoporous silica increased the adsorption efficiency. In general, amino groups are cationic species, and AB-40 is an anionic dye. In the water medium, the electrostatic interaction between positively charged $-NH_3^+$ and negatively charged AB-40 on the silica surface enhanced the dye adsorption (Park et al., 2020). Although pure SBA-15 had a larger surface area and pore volume (Table 1), N-SBA-15 provided stronger active sites for dye molecules, which was more suitable for adsorption. The results of the adsorption experiment also revealed that the adsorption capacity of N-SBA-15 for the three adsorbates decreased in the following order: TA > AB-40 > AR-1. Additionally, the adsorption rate rapidly increased at the initial time and then decreased after 60 min. The reason is that numerous active sites were available for TA and dyes adsorption from the beginning (Ali et al., 2022b). When the adsorption sites

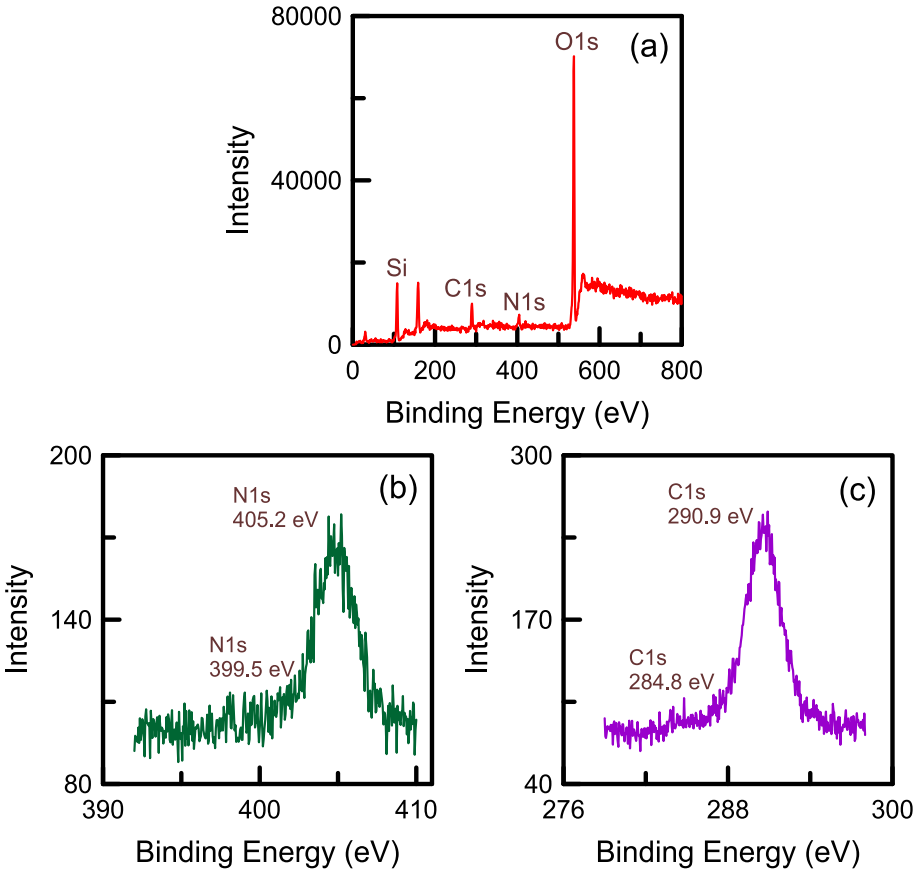

Fig. 8 XPS spectra of N-SBA-15: (a) survey spectrum, (b) N1s spectrum, and (c) C1s spectrum.

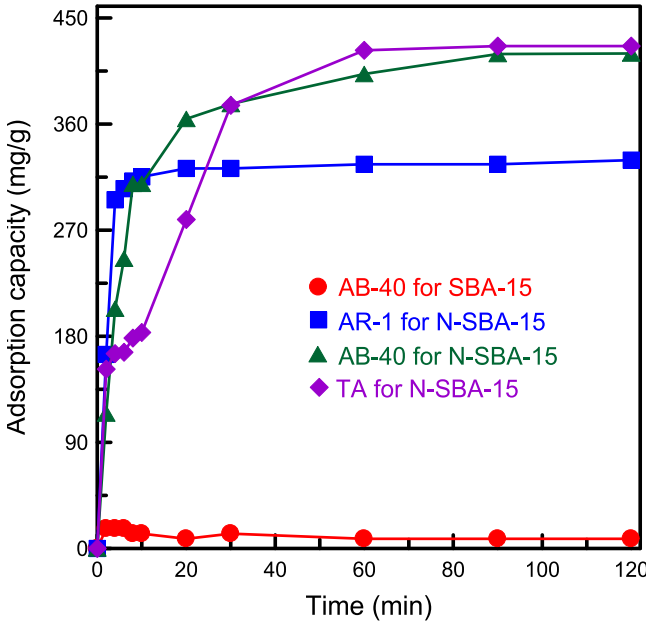

Fig. 9 Effect of contact time on degradation of TA and dye over SBA-15 and N-SBA-15 at equilibrium.

approached the saturation point after a certain time period, the resulting reduction in adsorption activity led to the slow diffusion of adsorbates into the SBA-15 mesopores. Additionally, the chemical bonding of nitrogen compounds has been inspected by FTIR and XPS apparatus (Fig. 7a and Fig. 8). These observations confirmed that amino groups were really conjugated with SBA-15. The leaching of amino groups from the surface of mesostructured silica in the solution could be neglected.

3.5.2. Effects of initial adsorbate concentration and adsorbent dosage

The initial concentrations of the adsorbates (TA, AR-1, and AB-40) were varied from 40 to 120 mg/L for N-SBA-15 adsorption, as shown in Fig. 10a and Fig. 10b. An increase in adsorbate concentration resulted in an increase in the adsorption capacity of N-SBA-15 (Fig. 10a). Typically, a higher initial concentration promoted a decrease in diffusion resistance between the solid and liquid phase, which facilitated the adsorption of more solute onto the solids, thereby enhancing the adsorption capacity. The same trend was observed by Babacan et al. (2022) for the removal of Reactive Red 120 and indigo carmine by using chitosan-based nanoparticles. As observed in Fig. 10b, the removal efficiency of AR-1 was enhanced by the use of a higher initial concentration. However, the removal efficiency of TA and AB-40 did not significantly increase in the studied concentration range. This result can be attributed to the saturation of the active sites on the N-SBA-15 surface during adsorption.

The N-SBA-15 dosage was changed from 5 to 25 mg for the adsorption of TA, AR-1, and AB-40, as illustrated in Fig. 10c

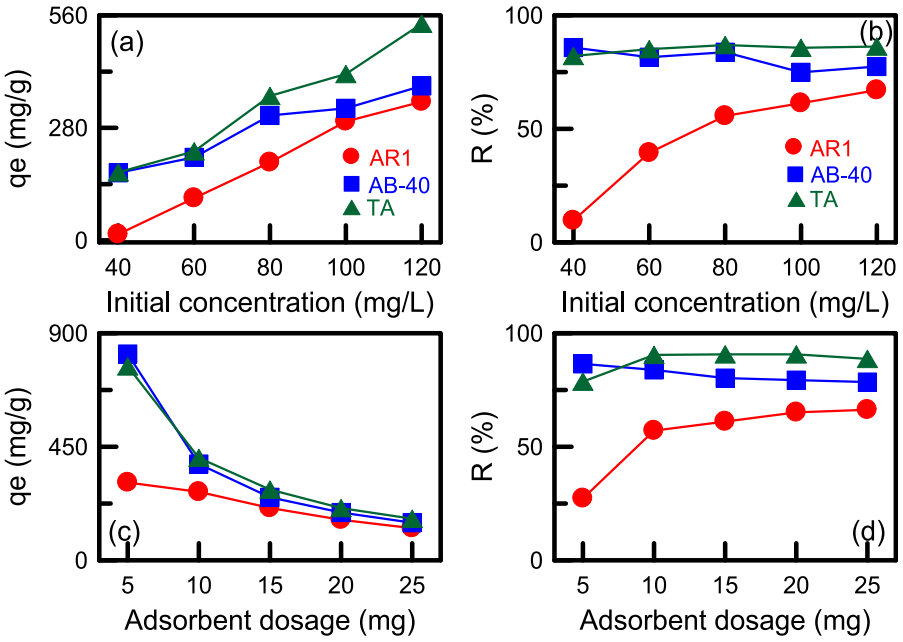

Fig. 10 Effect of (a), (b) initial concentration and (c), (d) N-SBA-15 dosage on the adsorption capacity and removal efficiency of N-SBA-15.

and Fig. 10d. The results revealed that an increase in N-SBA-15 mass resulted in a decrease in adsorption capacity and an increase in removal efficiency. The reduction in adsorption capacity was related to the excess adsorbent sites that were not completely used. This observation is consistent with the result obtained for the elimination of Congo red by poly(3-aminobenzoic acid/graphene oxide/cobalt ferrite) nanocomposite (P3ABA/GO/$CoFe_2O_4$) (Babakir et al., 2022). For TA, AB-40, and AR-1 adsorbates, N-SBA-15 exhibited the highest adsorption capacities of 869, 818, and 308 mg/g and maximum removal efficiencies of 92%, 87%, and 66%, respectively.

3.5.3. *Effects of solution pH and solution temperature*

The pH of a solution influences the ionization degree of organic pollutants and the surface charge of N-SBA-15, which are crucial to the adsorption process. Fig. 11a and Fig. 11b show the effect of pH on the efficiency of the adsorption of TA, AB-40, and AR-1 on N-SBA-15 materials. For AB-40 dye, the q_e and R values decreased with an increase in pH. AB-40 is an anionic adsorbate. In a strong acidic environment, the electrostatic attraction between the negative charged dye and positively charged sites favored dye adsorption (Abbood et al., 2023). For AR-1 dye, the q_e and R values decreased when the pH increased from 2 to 4. However, poor adsorption was observed when the pH was further increased from 4 to 12. This phenomenon may be attributable to the presence of the zwitterionic form of AR-1 dye at a pH of > 4.5. The reduction in electrostatic interaction caused a decrease in adsorption capacity and removal efficiency (Souza et al., 2021). For TA, high q_e and R values were observed at a pH of 4.0, which obviously decreased as the pH increased, approaching zero at pH values of 10 and 12. On the basis of the abovementioned results, the adsorption of TA, AR-1, and AB-40 was predominant in acidic media.

Temperature is a crucial factor for the adsorption process because it influences the repulsion and attraction between dye and solid. This study evaluated the adsorption activity of TA, AB-40, and AR-1 by using three temperatures (25, 35, and 45 °C). As shown in Fig. 11c and Fig. 11d, the q_e and R values gradually decreased with an increase in temperature. In particular, TA was relatively insensitive to temperature. The adsorption was typically an exothermic procedure; therefore, low temperatures favored adsorption. In general, the solubility of adsorbates on the solid surface may be enhanced when the solution temperature is increased. As a result, the attraction force between the solute and solid is reduced, leading to a decrease in adsorption activity. The same result was observed for the adsorption of methylene blue on tungsten oxide ($WO_{2.72}$) nanowires (Shang et al., 2019), with a temperature of 27 °C yielding better adsorption effects than a temperature range of 37–67 °C.

3.6. *Adsorption thermodynamics*

To compare the thermodynamic properties of TA, AB-40, and AR-1 adsorption on N-SBA-15, we calculated the Gibbs free energies (ΔG, kJ/mol) from the thermodynamic equilibrium constant (K_c) as follows (Albishri et al., 2023).

$$\Delta G = -RT \cdot \ln K_c \tag{3}$$

$$K_c = \frac{C_s}{C_e} \tag{4}$$

where T is the solution temperature (K), R is the gas constant (8.314 J/mol·K), and C_s and C_e (mg/L) are the concentrations of solutes at equilibrium on the solid and in the solution, respectively.

The standard entropy (ΔS, J/mol·K) and standard enthalpy (ΔH, kJ/mol) were obtained using the van't Hoff equation as follows:

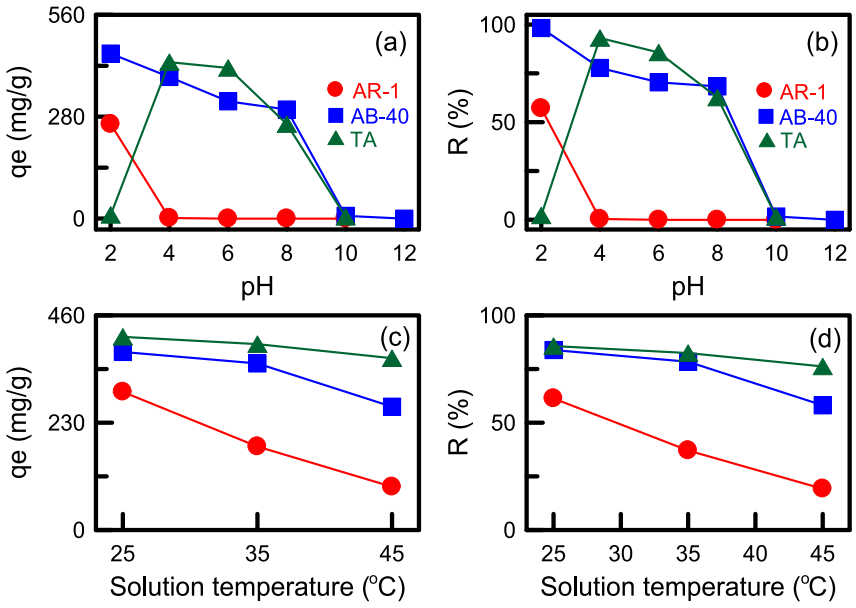

Fig. 11 Effect of (a), (b) solution pH and (c), (d) solution temperature on the adsorption capacity and removal efficiency of N-SBA-15 at equilibrium.

$$lnK_c = \frac{\Delta S}{R} - \frac{\Delta H}{RT} \quad (5)$$

The calculated thermodynamic parameters are provided in Table 2. For the three adsorbates (AR-1, AB-40, and TA), the negative ΔG values (−1.14 to − 4.43 kJ/mol) at 25 °C suggest the spontaneous behavior of the adsorption procedure. However, with an increase in the solution temperature, ΔG values also increased, indicating that the adsorption process was less favorable at high temperatures. The ΔG values decreased in the following order: AR-1 > AB-40 > TA, which corresponded to an increase in the adsorption capacity in the following order: AR-1 < AB-40 < TA (Fig. 9). This observation suggested that low free energy was favorable for the adsorption. The van't Hoff plots (Fig. 12) yielded negative values of ΔH (−75, −52, and − 25 kJ/mol), which verified the exothermic property. On the basis of the literature, an adsorption enthalpy < 40 kJ/mol generally indicated physisorption and higher energy (60–240 kJ/mol) indicated chemisorption (Banisheykholeslami et al., 2021). Accordingly, the TA adsorption process was mainly physisorption, and that of AR-1 was chemisorption. AB-40 adsorption was a combination of physisorption and chemisorption. The adsorption energies from different forces were indicated as follows: Van der Waals force (4 – 10 kJ/mol), hydrogen bond force (2 – 40 kJ/mol), and chemical bond force (> 60 kJ/mol) (Lin et al., 2011).

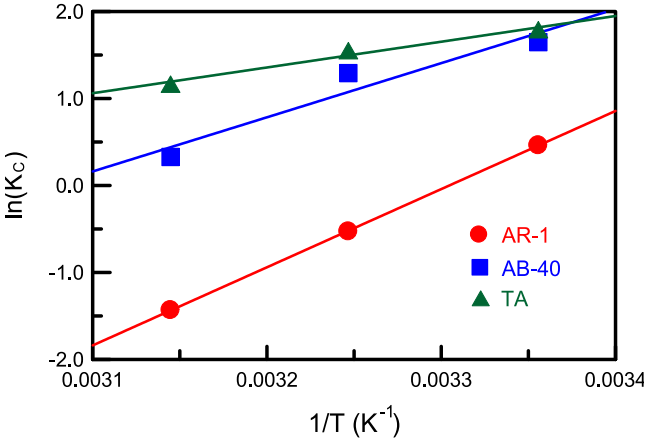

Fig. 12 Van't Hoff plots of TA and dye adsorption onto N-SBA-15.

The observation suggested that Van der Waals and hydrogen bond forces were also of importance to the adsorption process. The negative ΔS values (−67 to − 247 J/mol·K) implied that the collisions between the solute and N-SBA-15 interface were decreased during adsorption (Safarzadeh et al., 2022). The ΔH values were more negative in comparison with the ΔS values.

Table 2 Thermodynamic data for adsorption of TA and dyes on N-SBA-15.

Adsorbate	$\Delta\bar{S}$ (J/mol·K)	$\Delta\bar{H}$ (kJ/mol)	$\Delta\bar{G}$ (kJ/mol)		
			25℃	35℃	45℃
AR-1	−247	−75	−1.14	1.35	3.79
AB-40	−159	−52	−4.42	−3.31	−0.86
TA	−67	−25	−4.43	−3.97	−3.08

This conclusion confirmed that the adsorption was controlled by enthalpy, which provided more to the negative values of ΔG (Souza et al., 2021).

3.7. Adsorption isotherms

Adsorption isotherms are used to observe the interactions between the liquid and solid phases at equilibrium. Freundlich and Langmuir equations are the most commonly used models for analyzing adsorption isotherm parameters, adsorption type, and monolayer/multilayer adsorption. The adsorption was conducted by adding 10 mg of N-SBA-15 to 50 mL of TA, AB-40, and AR-1 solutions. The concentrations of the adsorbates were adjusted from 40 to 160 mg/L. The equilibrium temperature and time were 25 °C and 24 h, respectively.

The Langmuir and Freundlich equations are mathematically expressed as follows (Goswami and Dey, 2022):

$$\frac{1}{q_e} = \frac{1}{q_L} + \frac{1}{q_L K_L C_e} \tag{6}$$

$$logq_e = logK_F + \frac{1}{n} logC_e \tag{7}$$

where q_L (mg/g) is the maximum adsorption capacity, K_L (mL/mg) is the Langmuir constant, n and K_F are the Freundlich constants, and q_e (mg/g) is the adsorption capacity at equilibrium.

The linear plots of the two equations for AR-1, AB-40, and TA are presented in Fig. 13, and the fitted parameters are provided in Table 3. The correlation coefficient (R^2) was calculated to assess whether the optimal model fit the adsorptive data. For the three adsorbates, the Langmuir model revealed higher R^2 values than did the Freundlich model. The results suggested that the Langmuir model more accurately represented TA, AR-1, and AB-40 adsorption on N-SBA-15. The model assumed that the adsorption occurred on an adsorbent surface with a monolayer distribution of TA or dye molecules (Zhou et al., 2022b). The maximum adsorption capacities (q_L) for TA, AB-40, and AR-1 were 827.76, 543.04, and 476.24 mg/g, respectively. Finally, the R_L values (0.044–0.146) were in the range of 0–1, and the n values (1.71–4.30) were > 1, indicating that the adsorption process was favorable (Samiyammal et al., 2022). This may be attributable to the electrostatic attraction and π–π interaction between the amino groups and adsorbates.

3.8. Adsorption kinetics

Understanding the relevant adsorption mechanism is crucial to successful wastewater treatment. The removal of target pollutants by reaching adsorption equilibrium usually requires a short time period. Accordingly, the adsorption data were fitted using three models, namely pseudo-first-order, pseudo-second-order, and intraparticle diffusion models, which are described as follows (Kurnia et al., 2022):

$$q_t = q_e\left(1 - e^{-k_1 t}\right) \tag{8}$$

$$\frac{t}{q_t} = \frac{1}{k_2 q_e^2} + \frac{t}{q_e} \tag{9}$$

$$q_t = k_i t^{0.5} + I \tag{10}$$

where k_1 and k_2 are the rate constants, I is the boundary thickness, and k_i is the intraparticle diffusion rate constant.

The plots of q_t or t/q_t versus time based on Eqs. (8) and (9) for AR-1, AB-40, and TA adsorbates are presented in Fig. 14. The fitted parameters are provided in Table 4. For the three adsorbates, the pseudo-second-order model yielded higher R^2 values and therefore was a better fit to adsorptive data than

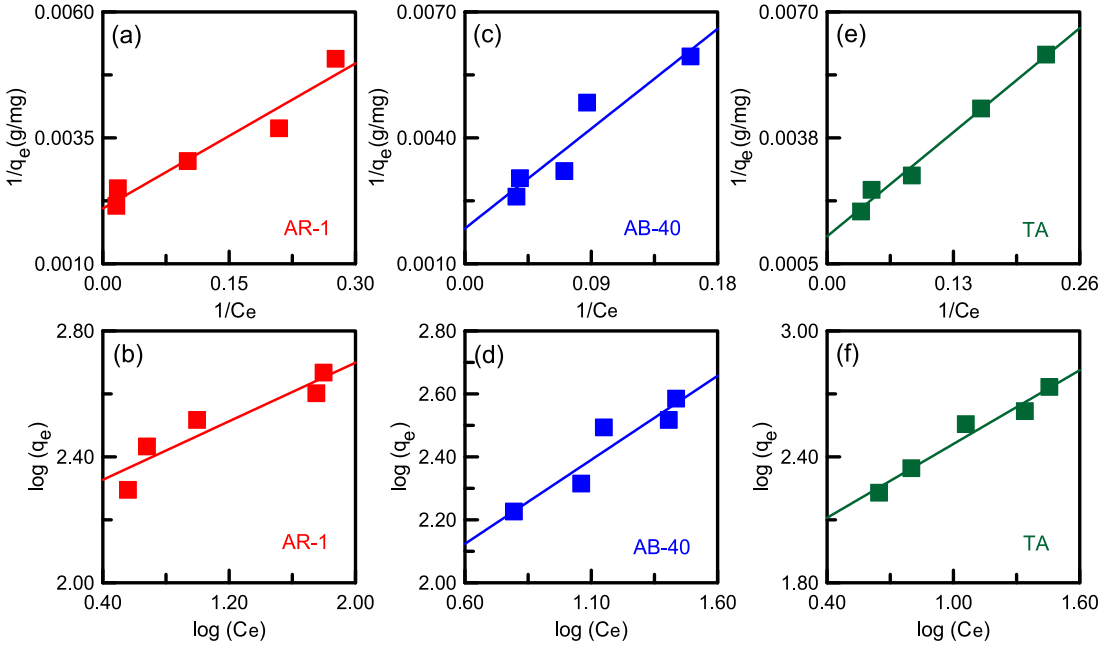

Fig. 13 Linear isotherm fittings for TA and dye adsorption onto N-SBA-15: (a), (c), (e) Langmuir model and (b), (d), (f) Freundlich model.

Table 3 Optimized isotherm data for adsorption of TA and dyes on N-SBA-15.

Sample	Langmuir				Freundlich		
	R_L	q_L (mg/g)	K_L	R^2	n	K_F (mg/g)	R^2
AR-1	0.044	476.24	0.219	0.9361	4.30	171.36	0.8729
AB-40	0.125	543.04	0.070	0.9050	1.87	63.56	0.8850
TA	0.146	827.76	0.058	0.9886	1.71	75.01	0.9641

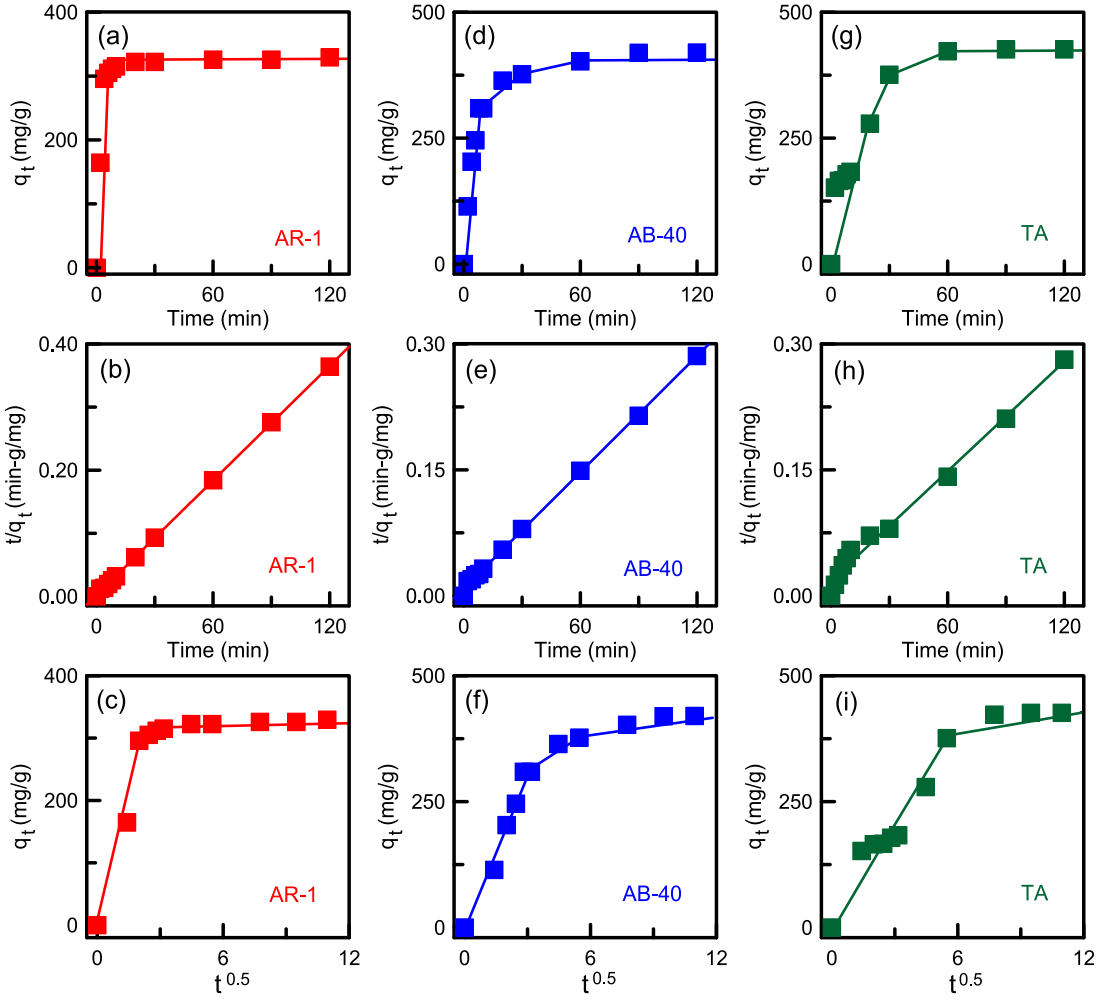

Fig. 14 Kinetics data fittings for TA and dye adsorption onto N-SBA-15: (a), (d), (g) pseudo-first-order model; (b), (e), (h) pseudo-second-order model; and (c), (f), (i) intraparticle diffusion model.

was the pseudo-first-order model. Moreover, the calculated adsorption capacities (330.03, 438.60, and 458.72 mg/g) were similar to the experimental adsorption capacities (329.41, 419.97, and 426.25 mg/g). Thus, the pseudo-second-order model was more suitable for the elimination of TA and dyes by using N-SBA-15.

As indicated in Fig. 14, the kinetic data for the intraparticle diffusion model as described using equation (10) are presented in Table 4. The presence of three linearity regions implied that the total adsorption process occurred in three steps. The first step involved the diffusion of TA or dye into the N-SBA-15 film. The second and third steps were extrapolated by the intraparticle diffusion and surface adsorption state, respectively. The rate constants were of the order $k_{i2} \ll k_{i1}$, which could be attributable to the longer time required for the diffusion of adsorbates into the silica pores, thus reducing the adsorption rate. Moreover, the k_{i3} values were small, indicating that the diffusion course was controlled by surface adsorption. A similar phenomenon was observed in the adsorption process of anionic azo dyes on activated carbon composites (Xue et al., 2023).

To further evaluate the suitability of N-SBA-15 as an adsorbent, we compared the maximum adsorption capacities of AR-1, AB-40, and TA for various adsorbents reported in

Table 4 Optimized kinetics data for adsorption of TA and dyes on N-SBA-15.

Model	Parameter	Value		
		AR-1	AB-40	TA
Pseudo-first-order adsorption kinetic	$q_{e,experiment}$ (mg/g)	329.41	419.97	426.25
	$q_{e,calculated}$ (mg/g)	325.81	402.93	419.70
	k_1 (min^{-1})	0.4310	0.1624	0.7371
	R^2	0.9862	0.9863	0.9213
Pseudo-second-order adsorption kinetic	$q_{e,experiment}$ (mg/g)	329.41	419.97	426.25
	$q_{e,calculated}$ (mg/g)	330.03	438.60	458.72
	k_2 (min^{-1})	0.0045	0.0006	0.0003
	R^2	0.9999	0.9993	0.9942
Intraparticle diffusion kinetic	k_{i1} (mg/g $min^{1/2}$)	142.06	104.56	82.76
	I_1	−8.30	−9.56	30.68
	k_{i2} (mg/g $min^{1/2}$)	16.95	29.91	55.79
	I_2	262.74	219.56	−82.31
	k_{i3} (mg/g $min^{1/2}$)	1.48	8.22	9.01
	I_3	313.33	335.58	336.97

Table 5 Comparison of adsorption capacity for different types of adsorbents.

Adsorbent	Adsorbate	q (mg/g)	Reference
Activated carbon	TA	162	Hsieh and Teng, 2000
Chitosan/NaOH/fly ash composite	TA	244	Agarwal et al., 2018
Porous crosslinked polystyrene	TA	248	Zhang et al., 2020
Biochar	TA	87	Lawal et al., 2021
Carbon xerogel	AB-40	245.5	Zhou et al., 2011
Cone biomass of Thuja orientalis	AB-40	97.06	Akar et al., 2008
Carbon sphere and layered double hydroxide composite	AR-1	342	Zhang et al., 2022b
Sugarcane bagasse-based biocomposites	AR-1	143.4–205.1	Kamran et al., 2022
Fe_3O_4/MIL-101(Cr)	AR-1	142.9	Wang et al., 2016
N-SBA-15	TA	869	Present work
N-SBA-15	AB-40	818	Present work
N-SBA-15	AR-1	308	Present work

the literature. Table 5 reveals that N-SBA-15 had higher adsorption capacities (308 mg/g for AR-1, 818 mg/g for AB-40, and 869 mg/g for TA) than those of the adsorbents in different studies. Accordingly, amino-functionalized SBA-15 could be regarded as a highly efficient adsorbent with a high surface area for the removal of organic pollutants from wastewater.

4. Conclusions

A multifunctional amino compound was developed by anchoring PEHA to mesoporous SBA-15 silica and applied as an adsorbent for TA and dye elimination. The composite had oxygen-containing functional groups, which enabled favorable adsorption through electrostatic attraction and π–π interaction with adsorbate molecules. The mesophase characteristics of SBA-15 were slightly affected by hydrothermal treatment temperature and time. Pore structure analysis indicated that both SBA-15 and N-SBA-15 samples demonstrated type IV isotherms, which belonged to a mesostructure. XPS and FTIR revealed that amino groups were deeply implanted on the surface of SBA-15. A combination of amino groups and SBA-15 can provide stronger active sites and consequently the adsorption capacity was effectively enhanced. For three adsorbates, the adsorption capacity decreased with increasing adsorbent dosage, solution pH and temperature. However, an increase in adsorbate concentration can enhance the adsorption capacity. Amino-modified SBA-15 exhibited maximum adsorption capacities of 308 mg/g for AR-1, 818 mg/g for AB-40, and 869 mg/g for TA, respectively. The pseudo-second-order and Langmuir models were the best fit for the adsorption of TA and dye onto N-SBA-15. The diffusion of adsorbates occurs in three steps, namely film diffusion, intraparticle diffusion into the N-SBA-15 pores, and surface adsorption, of which surface adsorption is the rate-determining step. The total adsorption was a highly spontaneous and exothermic process. In the future, we aim to perform the following: (i) add a magnetic material to modify the N-SBA-15 for facilitating the separation and recovery procedure; (ii) apply N-SBA-15 in the elimination of other contaminants such as heavy metals, herbicides, and hazardous dyes; (iii) enhance the stability and reusability of the adsorbent to lengthen its lifetime; (iv) employ N-SBA-15 for large-scale treatment of actual industrial wastewater.

CRediT authorship contribution statement

Zheng-Zhe Li: Supervision, Writing – review & editing. **Tzong-Horng Liou:** Methodology, Investigation, Writing – original draft. **Wen-Yang Liu:** Formal analysis, Validation. **Chun-Chia Hsu:** Resources, Data curation, Supervision. **Sheng-En Chiu:** Data curation, Supervision.

Declaration of Competing Interest

The authors declare that they have no known competing financial interests or personal relationships that could have appeared to influence the work reported in this paper.

Acknowledgments

The authors expressed thanks to the National Science and Technology Council (NSTC) of Taiwan for its financial supports under Project No. NSTC 112-2221-E-131-004.

References

Abbood, N.S., Ali, N.S., Khader, E.H., Majdi, H.S., Albayati, T.M., Saady, N.M.C., 2023. Photocatalytic degradation of cefotaxime pharmaceutical compounds onto a modified nanocatalyst. Res. Chem. Intermed. 49, 43–56.

Agarwal, S., Rajoria, P., Rani, A., 2018. Adsorption of tannic acid from aqueous solution onto chitosan/NaOH/fly ash composites: Equilibrium, kinetics, thermodynamics and modeling. J. Environ. Chem. Eng. 6 (1), 1486–1499.

Akar, T., Ozcan, A.S., Tunali, S., Ozcan, A., 2008. Biosorption of a textile dye (Acid Blue 40) by cone biomass of Thuja orientalis: Estimation of equilibrium, thermodynamic and kinetic parameters. Bioresour. Technol. 99, 3057–3065.

Alardhi, S.M., Alrubaye, J.M., Albayati, T.M., 2020. Removal of methyl green dye from simulated waste water using hollow fiber ultrafiltration membrane, 2020. IOP Conf. Ser.: Mater. Sci. Eng. 928, 052020.

Albishri, W.S., Katouah, H.A., 2023. Functionalization of sodium magnesium silicate hydroxide/sodium magnesium silicate hydrate nanostructures by chitosan as a novel nanocomposite for efficient removal of methylene blue and crystal violet dyes from aqueous media. Arabian J. Chem. 16, 104804.

Ali, N.S., Kalash, K.R., Ahmed, A.N., Albayati, T.M., 2022a. Performance of a solar photocatalysis reactor as pretreatment for wastewater via UV, UV/TiO2, and UV/H2O2 to control membrane fouling. Sci. Rep. 12, 16782.

Ali, N.S., Jabbar, N.M., Alardhi, S.M., Majdi, H.S., Albayati, T.M., 2022b. Adsorption of methyl violet dye onto a prepared bio-adsorbent from date seeds: isotherm, kinetics, and thermodynamic studies. Heliyon 8, e10276.

Al-Jaaf, H.J., Ali, N.S., Alardhi, S.M., Albayati, T.M., 2022. Implementing eggplant peels as an efficient bio-adsorbent for treatment of oily domestic wastewater. Desalin. Water Treat. 245, 226–237.

Al-Nayili, A., Majdi, H.S., Albayati, T.M., Saady, N.M.C., 2022. Formic acid dehydrogenation using noble-metal nanoheterogeneous catalysts: Towards sustainable hydrogen- based energy. Catalysts 12, 324.

Anbia, M., Salehi, S., 2012. Removal of acid dyes from aqueous media by adsorption onto amino-functionalized nanoporous silica SBA-3. Dyes Pigment. 94 (1), 1–9.

Atiyah, N.A., Albayati, T.M., Atiya, M.A., 2022. Interaction behavior of curcumin encapsulated onto functionalized SBA-15 as an efficient carrier and release in drug delivery. J. Mol. Struct. 1260, 132879.

Babacan, T., Doğan, D., Erdem, Ü., Metin, A.Ü., 2022. Magnetically responsive chitosan-based nanoparticles for remediation of anionic dyes: Adsorption and magnetically triggered desorption. Mater. Chem. Phys. 284, 126032.

Babakir, B.A.M., Ali, L.I.A., Ismail, H.K., 2022. Rapid removal of anionic organic dye from contaminated water using a poly(3-aminobenzoic acid/graphene oxide/cobalt ferrite) nanocomposite low-cost adsorbent via adsorption techniques. Arab. J. Chem. 15, (12) 104318.

Banisheykholeslami, F., Hosseini, M., Darzi, G.N., 2021. Design of PAMAM grafted chitosan dendrimers biosorbent for removal of anionic dyes: Adsorption isotherms, kinetics and thermodynamics studies. Int. J. Biol. Macromol. 177, 306–316.

Bi, F., Zhao, Z., Yang, Y., Gao, W., Liu, N., Huang, Y., Zhang, X., 2022. Chlorine-coordinated Pd single atom enhanced the chlorine resistance for volatile organic compound degradation: mechanism study. Environ. Sci. Technol. 56, 17321–17330.

Bi, F., Ma, S., Gao, B., Yang, Y., Wang, L., Fei, F., Xu, J., Huang, Y., Wu, M., Zhang, X., 2023. Non-oxide supported Pt-metal-group catalysts for efficiently CO and toluene co-oxidation: Difference in water resistance and degradation intermediates. Fuel 344, 128147.

Chen, Y., Huang, Y., 2023. Influence of ceria existence form on deactivation behavior of Cu-Ce/SBA-15 catalysts for methanol steam reforming. Int. J. Hydrog. Energy 48 (4), 1323–1336.

Fei, X., Chen, S., Liu, D., Huang, C., Zhang, Y., 2016. Comparison of amino and epoxy functionalized SBA-15 used for carbonic anhydrase immobilization. J. Biosci. Bioeng. 122 (3), 314–321.

Gao, S., Li, X., Bao, X., Chen, K., Liu, X., Qian, F., Shen, X., 2020. Preconcentration of allergenic disperse dyes in environmental water samples based on amino functionalized metal–organic framework. Microchem J. 157, 105059.

Goswami, R., Dey, A.K., 2022. Synthesis and application of treated activated carbon for cationic dye removal from modelled aqueous solution. Arabian J. Chem. 15, 104290.

Hsieh, C.T., Teng, H., 2000. Influence of mesopore volume and adsorbate size on adsorption capacities of activated carbons in aqueous solutions. Carbon 38 (6), 863–869.

Jabbar, N.M., Alardhi, S.M., Mohammed, A.K., Salih, I.K., Albayati, T.M., 2022. Challenges in the implementation of bioremediation processes in petroleum-contaminated soils: A review. Environ. Nanotechnol. Monit. Manag. 18, 100694.

Kadhum, S.T., Alkindi, G.Y., Albayati, T.M., 2021. Determination of chemical oxygen demand for phenolic compounds from oil refinery wastewater implementing different methods. Desalin. Water Treat. 231, 44–53.

Kalhor, M.M., Rafati, A.A., Rafati, L., Rafati, A.A., 2018. Synthesis, characterization and adsorption studies of amino functionalized silica nano hollow sphere as an efficient adsorbent for removal of imidacloprid pesticide. J. Mol. Liq. 266, 453–459.

Kamran, U., Bhatti, H.N., Noreen, S., Tahir, M.A., Park, S.J., 2022. Chemically modified sugarcane bagasse-based biocomposites for efficient removal of acid red 1 dye: Kinetics, isotherms, thermodynamics, and desorption studies. Chemosphere 291, 132796.

Kurnia, K.A., Rahayu, A.P., Islami, A.F., Kusumawati, Y., Wenten, I.G., Saepurahman, A.U.R., Wellia, D.V., Saefumillah, A., 2022. Insight into the adsorption of dyes onto chitin in aqueous solution: An experimental and computational study. Arabian J. Chem. 15, 104293.

Lawal, A.A., Hassan, M.A., Zakaria, M.R., Yusoff, M.Z.M., Norrrahim, M.N.F., Mokhtar, M.N., Shirai, Y., 2021. Effect of oil palm biomass cellulosic content on nanopore structure and adsorption capacity of biochar. Bioresour. Technol. 332, 125070.

Li, H., Yu, J., Gong, Y., Lin, N., Yang, Q., Zhang, X., Wang, Y., 2023. Perovskite catalysts with different dimensionalities for environmental and energy applications: A review. Sep. Purif. Technol. 307, 122716.

Lin, H., Jie, B., Ye, J., Zhai, Y., Luo, Z., Shao, G., Chen, R., Zhang, X., Yang, Y., 2023. Recent advance of macroscopic metal-organic frameworks for water treatment: A review. Surf. Interfaces 36, 102564.

Lin, J., Zhan, Y., Zhu, Z., Xing, Y., 2011. Adsorption of tannic acid from aqueous solution onto surfactant-modified zeolite. J. Hazard. Mater. 193, 102–111.

Liou, T.H., Tseng, Y.K., Liu, S.M., Lin, Y.T., Wang, S.Y., Liu, R.T., 2021. Green synthesis of mesoporous graphene oxide/silica

nanocomposites from rich husk ash: Characterization and adsorption performance. Environ. Technol. Innov. 22, 101424.
Liou, T.H., Liu, S.M., Chen, G.W., 2022. Utilization of e-wastes as a sustainable silica source in synthesis of ordered mesostructured titania nanocomposites with high adsorption and photoactivity. J. Environ. Chem. Eng. 10, (2) 107283.
Liou, T.H., Tseng, Y.K., Zhang, T.Y., Liu, Z.S., Chen, J.Y., 2023. Rice husk char as a sustainable material for the preparation of graphene oxide-supported biocarbons with mesoporous structure: A characterization and adsorption study. Fuel 344, 128042.
Liu, F., Wang, A., Xiang, M., Hu, Q., Hu, B., 2022. Effective adsorption and immobilization of Cr(VI) and U(VI) from aqueous solution by magnetic amine-functionalized SBA-15. Sep. Purif. Technol. 282, 120042.
Osagie, C., Othmani, A., Ghosh, S., Malloum, A., Esfahani, Z.K., Ahmadi, S., 2021. Dyes adsorption from aqueous media through the nanotechnology: A review. J. Mater. Res. Technol. 14, 2195–2218.
Park, J.A., Kang, J.K., Jung, S.M., Choi, J.W., Lee, S.H., Yargeau, V., Kim, S.B., 2020. Investigating Microcystin-LR adsorption mechanisms on mesoporous carbon, mesoporous silica, and their amino-functionalized form: Surface chemistry, pore structures, and molecular characteristics. Chemosphere 247, 125811.
Perrotti, T.C., Freitas, N.S., Alzamora, M., Sánchez, D.R., Carvalho, N.M.F., 2019. Green iron nanoparticles supported on amino-functionalized silica for removal of the dye methyl orange. J. Environ. Chem. Eng. 7, (4) 103237.
Rajabi, Z., Javanbakht, M., Hooshyari, K., Adibi, M., Badiei, A., 2021. Phosphoric acid doped polybenzimidazole based polymer electrolyte membrane and functionalized SBA-15 mesoporous for elevated temperature fuel cell. Int. J. Hydrog. Energy 46 (66), 33241–33259.
Razak, N.A.A., Othman, N.H., Shayuti, M.S.M., Jumahat, A., Sapiai, N., Lau, W.J., 2022. Agricultural and industrial waste-derived mesoporous silica nanoparticles: A review on chemical synthesis route. J. Environ. Chem. Eng. 10, (2) 107322.
Sadeghi, M., Moradian, M., Tayebi, H.A., Mirabi, A., 2023. Removal of Penicillin G from aqueous medium by PPI@SBA-15/ZIF-8 super adsorbent: Adsorption isotherm, thermodynamic, and kinetic studies. Chemosphere 311, 136887.
Sadou, M., Saadi, A., Meliani, M.H., Suleiman, R.K., Saleh, T.A., 2022. Facile Preparation of Supported Copper-modified SBA-15 Catalysts for efficient Benzaldehyde Hydrogenation. Surf. Interfaces 30, 101955.
Safarzadeh, H., Peighambardoust, S.J., Mousavi, S.H., Foroutan, R., Mohammadi, R., Peighambardoust, S.H., 2022. Adsorption ability evaluation of the poly(methacrylic acid-co-acrylamide)/cloisite 30B nanocomposite hydrogel as a new adsorbent for cationic dye removal. Environ. Res. 212, 113349.
Samiyammal, P., Kokila, A., Pragasan, L.A., Rajagopal, R., Sathya, R., Ragupathy, S., Krishnakumar, M., Reddy, V.R.M., 2022. Adsorption of brilliant green dye onto activated carbon prepared from cashew nut shell by KOH activation: Studies on equilibrium isotherm. Environ. Res. 212, 113497.
Sfeir, A., Teles, C.A., Ciotonea, C., Reddy, G.N.M., Marinova, M., Dhainaut, J., Löfberg, A., Dacquin, J.P., Royer, S., Laassiri, S., 2023. Enhancing ammonia catalytic production over spatially confined cobalt molybdenum nitride nanoparticles in SBA-15. Appl. Catal. B-Environ. 325, 122319.
Shang, Y., Cui, Y., Shi, R., Yang, P., Wang, J., Wang, Y., 2019. Regenerated $WO_{2.72}$ nanowires with superb fast and selective adsorption for cationic dye: Kinetics, isotherm, thermodynamics, mechanism. J. Hazard. Mater. 379, 120834.
Shi, Y., Chang, Q., Zhang, T., Song, G., Sun, Y., Ding, G., 2022. A review on selective dye adsorption by different mechanisms. J. Environ. Chem. Eng. 10, (6) 108639.
Souza, A.P.N., Licea, Y.E., Colaço, M.V., Senra, J.D., Carvalho, N. M.F., 2021. Green iron oxides/amino-functionalized MCM-41 composites as adsorbent for anionic azo dye: Kinetic and isotherm studies. J. Environ. Chem. Eng. 9, (2) 105062.
Ulagesan, S., Santhamoorthy, M., Phan, T.T.V., Alagumalai, K., Thirupathi, K., Kim, S.C., Nam, T.J., Choi, Y.H., 2022. Mesoporous silica (SBA-15) with enriched amidoxime functionalities for pH-controlled anticancer drug delivery. Inorg. Chem. Commun. 146, 110132.
Vargas-Osorio, Z., Klotschan, A., Arango-Ospina, M., Piñeiro, Y., Liverani, L., Rivas, J., Michálek, M., Galusek, D., Boccaccini, A. R., 2022. Effect of glycerol and H_3PO_4 on the bioactivity and degradability of rod-like SBA-15 particles with active surface for bone tissue engineering applications. Microporous Mesoporous Mat. 329, 111543.
Wang, Y., Gong, Y., Lin, N., Yu, L., Du, B., Zhang, X., 2022. Enhanced removal of Cr(VI) from aqueous solution by stabilized nanoscale zero valent iron and copper bimetal intercalated montmorillonite. J. Colloid Interface Sci. 606, 941–952.
Wang, Y., Anyanwu, J.T., Hu, Z., Yang, R.T., 2023a. Significantly enhancing CO_2 adsorption on Amine-Grafted SBA-15 by boron doping and acid treatment for direct air capture. Sep. Purif. Technol. 309, 123030.
Wang, S., Zhang, Q., Cui, C., Niu, H., Wu, C., Wang, J., 2023b. Ionic liquids-SBA-15 hybrid catalysts for highly efficient and solvent-free synthesis of diphenyl carbonate. Green Energy Environ. 8 (1), 183–193.
Wang, T., Zhao, P., Lu, N., Chen, H., Zhang, C., Hou, X., 2016. Facile fabrication of Fe_3O_4/MIL-101(Cr) for effective removal of acid red 1 and orange G from aqueous solution. Chem. Eng. J. 295, 403–413.
Xue, H., Gao, X., Seliem, M.K., Mobarak, M., Dong, R., Wang, X., Fu, K., Li, Q., Li, Z., 2023. Efficient adsorption of anionic azo dyes on porous heterostructured MXene/biomass activated carbon composites: Experiments, characterization, and theoretical analysis via advanced statistical physics models. Chem. Eng. J. 451, 38735.
Yang, Y., Zhao, S., Bi, F., Chen, J., Li, Y., Cui, L., Xu, J., Zhang, X., 2022. Oxygen-vacancy-induced O_2 activation and electron-hole migration enhance photothermal catalytic toluene oxidation. Cell Rep. Phys. Sci. 3, 101011.
Yin, X., Teng, A., Zeng, Z., Meng, H., Wu, W., 2022. Facile and novel preparation of 2D-MoS_2/carbon nanodots composite with high adsorption efficiency and capacity for dye removal. Chem. Eng. J. 450, 138319.
Yu, J., Li, H., Lin, N., Gong, Y., Jiang, H., Chen, J., Wang, Y., Zhang, X., 2023. Oxygen-deficient engineering for perovskite oxides in the application of AOPs: regulation, detection, and reduction mechanism. Catalysts 13, 148.
Zhang, Z., Li, H., Liu, H., 2018. Insight into the adsorption of tetracycline onto amino and amino–Fe^{3+} gunctionalized mesoporous silica: Effect of functionalized groups. J. Environ. Sci. 65, 171–178.
Zhang, J.W., Nur'aini, A.D., Wang, Y.C., Hai, N.D., Minh, D.V., Cha, H.P., 2022b. Multiple pollutants removal by carbon sphere and layered double hydroxide composites: Adsorption behavior and mechanisms. J. Environ. Chem. Eng. 10, (3) 108014.
Zhang, K., Wang, Q., Zhou, Y., Gao, J., Li, C., Jiang, X., 2020. A low-cost crosslinked polystyrene derived from environmental wastes for adsorption of phenolic compounds from aqueous solution. J. Mol. Liq. 314, 113641.
Zhang, Y., Zhang, C., Liu, G., Wang, L., Pan, Z., 2023b. Ce-doped SBA-15 supported Pd catalyst for efficient hydrogenation of 2-ethyl-anthraquinone. Appl. Surf. Sci. 616, 156515.
Zhang, Y., Wang, W., Liu, C., Shen, P., Liu, Z., Hu, J., Shi, F., 2023c. Facile synthesis of HPW@MOF-199 embedded in SBA-15 functionalized with -COOH groups as a steady catalyst for the esterification reaction. Fuel 340, 127563.
Zhang, X., Zhao, Z., Zhao, S., Xiang, S., Gao, W., Wang, L., Xu, J., Wang, Y., 2022a. The promoting effect of alkali metal and H_2O on

Mn-MOF derivatives for toluene oxidation: A combined experimental and theoretical investigation. J. Catal. 415, 218–235.
Zhang, X., Liu, Z., Huang, Y., Niu, Y., Zhang, L., Xiong, T., Zhang, Y., Zhang, R., Zhang, H., 2023a. Preparation and in vitro evaluation of hesperidin nanoparticles by antisolvent recrystallization in a double homogenate system. Food Chem. X 18, 100639.
Zhou, S., Jin, L., Gu, P., Tian, L., Li, N., Chen, D., Marcomini, A., Xu, Q., Lu, J., 2022b. Novel calixarene-based porous organic polymers with superfast removal rate and ultrahigh adsorption capacity for selective separation of cationic dyes. Chem. Eng. J. 433, 134442.
Zhou, G., Tian, H., Sun, H., Wang, S., Buckley, C.E., 2011. Synthesis of carbon xerogels at varying sol–gel pHs, dye adsorption and chemical regeneration. Chem. Eng. J. 171, 1399–11140.
Zhou, G., Yang, S., Tian, Y., Liu, Y., Liu, Z., Dong, X., 2022a. Adsorption application of tetraethylenepentamine (TEPA) modified SBA-15@MIL-101(Cr) in carbon capture and storage (CCS). Microporous Mesoporous Mat. 344, 112232.